

Article

Quantitative Characterization of Interfacial Defects in Thermal Barrier Coatings by Long Pulse Thermography

Jinfeng Wei ^{1,2,†}, Guangnan Xu ^{1,†}, Guolin Liu ¹, Jinwei Guo ^{1,*}, Wang Zhu ^{1,*}  and Zengsheng Ma ¹ ¹ School of Materials Science and Engineering, Xiangtan University, Xiangtan 411105, China² Hunan Aviation Powerplant Research Institute, Aero Engine Corporation of China, Zhuzhou 412000, China

* Correspondence: jwguo@xtu.edu.cn (J.G.); wzhu@xtu.edu.cn (W.Z.)

† These authors contributed equally to this work.

Abstract: The non-contact long pulse thermography method is commonly used to detect the defects in thermal barrier coatings (TBCs). The profile of interfacial defect in TBCs can be monitored by infrared camera under the irradiation of the excitation source. Unfortunately, the defect profile is always blurry due to heat diffusion between the defect area and the intact area. It is difficult to quantify the size of defect size in TBCs. In this work, combined with derived one-dimensional heat conduction analytical model, a non-contact long pulse thermography (LPT) method is applied to quantitatively investigate the interface defects in TBCs. Principal component analysis (PCA) and background subtraction method are used to improve the contrast of the defect profile in collected thermal images. By fitting the results between the profile of the interface defect in thermal images and the predicted shape of the model, the interface defect size can be determined. Furthermore, a simple extension of proposed method for interfacial defects with irregular shape is presented. The predicted errors for round defect with diameters of 3 mm, 5 mm and 7 mm are roughly distributed in the range of 3%~6%, which are not affected by the defect diameter.

Keywords: thermal barrier coatings; long pulse thermography; interfacial defects; fitting background subtraction; quantitative characterization



Citation: Wei, J.; Xu, G.; Liu, G.; Guo, J.; Zhu, W.; Ma, Z. Quantitative Characterization of Interfacial Defects in Thermal Barrier Coatings by Long Pulse Thermography. *Coatings* **2022**, *12*, 1829. <https://doi.org/10.3390/coatings12121829>

Academic Editor: Cecilia Bartuli

Received: 27 October 2022

Accepted: 23 November 2022

Published: 26 November 2022

Publisher's Note: MDPI stays neutral with regard to jurisdictional claims in published maps and institutional affiliations.



Copyright: © 2022 by the authors. Licensee MDPI, Basel, Switzerland. This article is an open access article distributed under the terms and conditions of the Creative Commons Attribution (CC BY) license (<https://creativecommons.org/licenses/by/4.0/>).

1. Introduction

Thermal barrier coatings (TBCs) are widely used to improve the temperature-bearing capacity of high temperature components in aircraft engines such as high pressure turbine blades and combustors [1,2]. A typical system of TBCs is composed of a superalloy substrate, a ceramic topcoat with low thermal conductivity, and a metallic bond coat for offering adhesion between the topcoat and the substrate [3–6]. In addition, thermally grown oxide (TGO) is formed in the interface between the ceramic topcoat (TC) and bond coat (BC) due to oxidation at high temperature [7]. TBCs can effectively provide reductions in the surface temperature of the superalloy substrate (100–300 °C) [8]. Due to the complex multi-layer structures of TBCs and the harsh service environment, the coating is prone to interfacial defects such as debonding and buckling. Further propagation of these defects will lead to spalling failure of TBCs, which seriously threatens the safe application of TBCs on turbine blades. Many previous studies show that the spallation of TBCs starts as a separation between TC and BC. Zhen et al. [9] found that delamination cracking appears in the interior of the TGO layer and the interface area between BC and TGO layers after thermal cycling. Wei et al. [10] showed that the surface vertical crack expands to the interface of BC/TGO layers and merges rapidly with the horizontal crack, with the consideration of TGO growth and ceramic sintering. As the delamination between TC and BC becomes large enough, buckling appears [11,12], and enough buckling will cause the spalling of TC. However, some interfacial defects are buried in the bottom of the ceramic coating, which are hard to directly observe with the naked eye. In order to avoid sudden

accidents and loss due to the detachment of TBCs, it is very important to develop an effective way to predict and evaluate the state of defect in TBCs.

Over the years, several nondestructive techniques such as ultrasonic [13], impedance spectroscopy [14], X-ray computed tomography [15,16], and infrared thermography non-destructive testing [17,18] have been used to evaluate and identify the state of defect in TBCs. Impedance spectroscopy and ultrasonic testing are the contact detection methods, and they are not conducive to defect detection for TBCs in many in-service situations. X-ray computed tomography is able to analyze the 3D spatial microstructure in nondestructive mode, but the inspection equipment is relatively costly, and the top ceramic coating need to be removed from the superalloy substrate for alleviating the effect of X-ray absorption. The above mentioned nondestructive testing methods are not ideal for the quantitative characterization of internal defects in TBCs. Infrared thermography testing has become a hot defect evaluation method due to the advantages of non-contact, high efficiency, direct detection results, and quantitative characterization of defects [19].

Long pulsed thermography (LPT) is commonly used to detect internal defects [20]. The detection principle of infrared thermography is that the excitation source (such as flash bulbs, halogen lamps) heats the surface of the sample and the temperature change of the sample surface is monitored and recorded by an infrared camera. Due to the difference of the thermal properties of defective and intact region, the temperature in the defective region is different from that in the intact region. Then, the information of defects can be detected, such as debond, crack, uneven thickness of coating, delamination and so on. Newaz et al. [21] investigated the progressive damage assessment in TBCs using PT technique, and the results verified that coating layering and buckling happens only toward the end of life and has a very short span. Combining Terahertz-Time domain spectroscopy (THz-TDS) with the PT technique, the degree of degradation of the thickness of TBCs top coat of varying service lifespans were quantitatively analyzed [22]. Based on the thermography method, Kumar et al. [23] collected the thermographic images of TBCs samples exposed to thermal cycling. The experimental results are consistent with the FEM results, which verified the delamination form of defect. Shi et al. [24] developed one-way coupling algorithm (GEMSS) and carried out the investigation of the thermal image collected by infrared thermography to detect cracks in TBCs. The amount and position of crack with different lengths can be identified from collected thermal image. Zhu et al. [25] combined the acoustic emission method with infrared thermography to explore the degradation mechanism of TBCs corroded by CMAS under thermal shock. The increased abnormal temperature area with the number of thermal shock cycles can be observed from the thermal images. The abnormal area was recognized as the spalling location.

Recently, a few quantitative evaluation methods of internal defect size have been developed for TBCs. Zhuo et al. [26] developed a size estimation method of interior defects, which added a hypothetical heat flux supplied from surface temperature measured by step heating thermography. Guo et al. [27] studied the diameter of in-plane defect by LPT, and proposed a novel method FWHM-1st to quantify the diameter. The error of their measurement results of defect becomes larger with the decrease in the defect size, and the minimum error reached 12%. Due to the inevitable fact that heat diffusion blurs the defect boundary in thermal images, the accurate evaluation of the sizes of smaller defects still needs to be developed.

In order to further enhance the assessment ability of the size of interfacial defects in thermal images of TBCs, we proposed a quantification method by fitting the results between the profile of interface defect in thermal images and the predicted shape of the model in this paper. First, LPT was used to quantitative investigate the interfacial defects of TBCs. Then, PCA is applied to extract a reconstructed thermal image from the abundant thermal images collected by LPT. The background subtraction method was used to reduce the background influence in the collected thermal images. Furthermore, a one-dimensional heat conduction analytical model of TBCs with interface defects was derived. By fitting the results between the profile of interface defect in thermal images and the predicted shape of

the model, the interface defect size can be determined. At last, a simple extension of current evaluation method of defect size was presented for interfacial defects with irregular shape.

2. Experiments

2.1. Sample

Two flat-plate test samples with the dimensions of 115 mm × 40 mm × 5 mm were prepared for the experiment. Each sample was composed of the stainless steel substrate, precast brass defects, and 7 wt.% yttria-stabilised zirconia (YSZ) coating. In order to produce interfacial defects in the samples, several cylindrical holes with different diameters and the same depth of 1.5 mm were drilled in the stainless steel substrate before spraying. Then, these holes were plugged with copper, which had the same dimensions as holes. The height of copper billet was slightly less than the depth of the cylindrical holes, therefore, a paper-thin air gap existed in the interface between the copper billet and stainless steel. Then, the surface of the stainless steel substrate was polished flat. Finally, the YSZ coating with a thickness of 200 μm was prepared on the surface of the substrate by air plasma spraying. The processing parameters for spraying the YSZ coating are given in Table 1.

Table 1. Spraying parameter for YSZ coat.

Voltage (V)	Current(A)	Primary Gas Ar (slpm)	Primary Gas H ₂ (slpm)	Standoff Distance (mm)	Feed Rate (g/min)
75	600	40	15	110	20

Sample 1 is used to propose the image processing method and the quantitative method of the size of defect. Sample 2 is used to verify the quantitative method. Figure 1 shows the schematic diagram of the dimension of the sample 1. The center of defects was in the bisector of substrate. The samples with different sizes of defects were used to investigate the effect of defect diameters on temperature distribution law. The dimensions of the in-plane defects are given in Table 2.

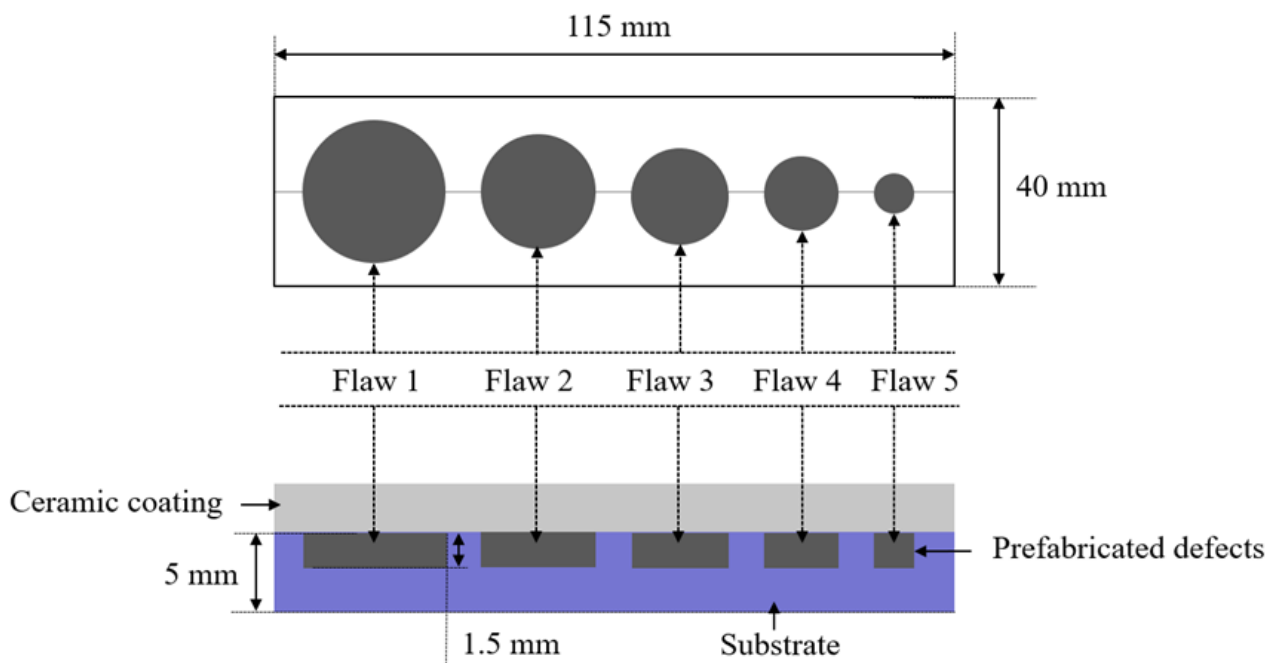


Figure 1. The schematic diagram of the dimension of the sample 1.

Table 2. Thickness of ceramic coating and the dimension of the interfacial defects.

Sample Number	Diameter of Defect D (mm)
1	Flaw 1: 10; Flaw 2: 8; Flaw 3: 6; Flaw 4: 4; Flaw 5: 2
2	Flaw 1: 7; Flaw 2: 5; Flaw 3: 3

2.2. Experimental Setup and Data Collection

A flow diagram of defect detection by LPT is shown in Figure 2. Two halogen lamps with a high power of 2 kW were selected as the excitation sources. In order to reduce the effect of uneven heating, the two lamps were placed symmetrically on both sides of the test sample, and the space between them was about 1 m. An infrared camera was put in the middle of the two lamps to capture the temperature evolution of samples surface. The objective table was used to place the tested sample, and located at the right ahead of the infrared camera. The spectral range, thermal sensitivity at room temperature and resolution of the infrared camera were 3.8~4.05 μm , 25 mK, and 320×240 pixels, respectively. In this study, the sampling frequency was 30 Hz, the heating time was 6 s, and the distance between the sample and the infrared camera was 30 cm.

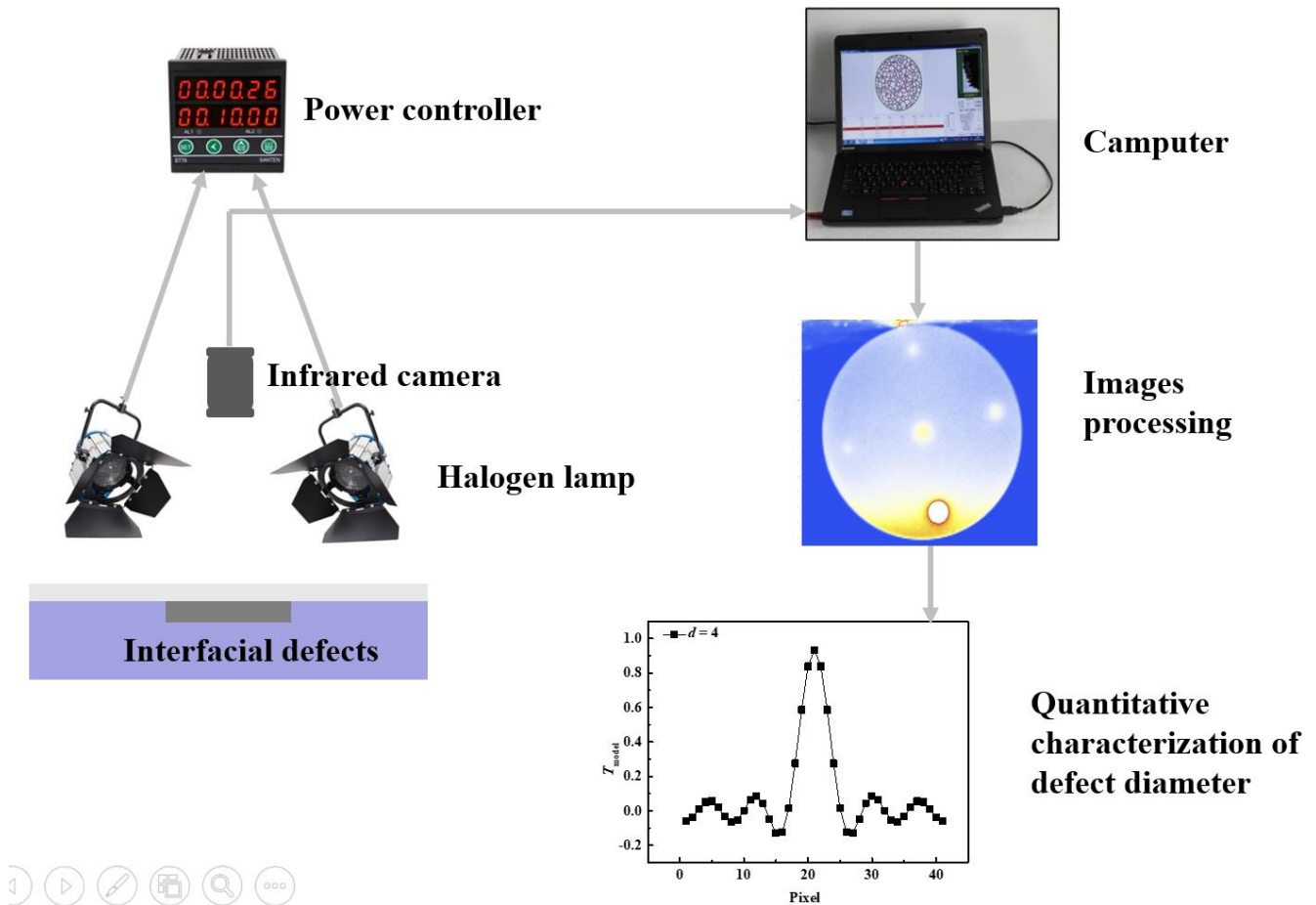


Figure 2. A flow diagram of defect detection by LPT.

Figure 3 shows an infrared image of the sample surface captured by the infrared camera. The temperature of the defective area was higher than that of the intact area. The 90 frames thermal images in the first 3 s period after removing the thermal excitation source were used to analyze the characteristic information of temperature. In order to reduce the effect of environmental noise on the defect identification, the first frame of the images was used as the background image, and the reconstructed 90 frames thermal sequence

images were obtained by subtracting background image from the images, including noise interference signal. To facilitate the following processing, the ratio (\bar{T}) of temperature data T extracted from the subtracting background thermal sequence image to T_d ($T_d = 1^\circ\text{C}$) was obtained.

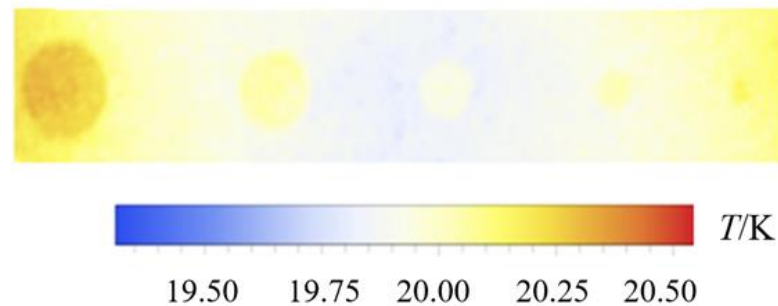


Figure 3. Thermal data captured by an infrared camera.

2.3. Principal Component Analysis (PCA)

PCA was used to process thermal image sequences with uneven heating noise and improve the defect detectability from multiple frames figures [28,29]. Based on the principle of data dimensionality reduction reconstruction, PCA uses the singular value decomposition (SVD) to extract the spatial and temporal information containing defect features from abundant thermal image sequences [28,30]. The SVD is written as follows:

$$[A] = [U][R][V]^T \quad (1)$$

where $[A]$ is a matrix, whose column vector is composed by each frame image compressed into a single column. $[U]$ and $[V]$ are the left and right singular matrixes of the matrix $[A]$. $[R]$ is a 90×90 diagonal matrix with the singular values of matrix $[A]$ in the diagonal and the elements of matrix $[R]$ are equal to zero on off-diagonal lines. Considering that data matrix $[A]$ is arranged time variations occur column-wise and spatial variations occur row-wise, the columns of matrix $[U]$ are composed by the empirical orthogonal functions (EOF) that can describe the spatial variables of the thermal response data. Matrix $[V]$ can describe the characteristic time behavior, where the principal component (PC) vectors are arranged row-wise [31,32].

Corresponding to the three principal components of the 90 frames of thermal images processed in previous section, the reconstructed thermal sequence images by PCA algorithm are shown in Figure 4. Conveniently, we denoted the reconstructed image of the n principal component as PCn . The temperature distribution in PCn is denoted by T_{PCn} . Figure 4a shows that a reconstructed thermal sequence image of the first principal corresponds to the three principal components of the 90 frames thermal images processed in the previous section; the reconstructed thermal sequence images by PCA algorithm are shown in Figure 4. Conveniently, we denoted the reconstructed image of the n principal component as PCn . The temperature distribution in PCn is denoted by T_{PCn} . Figure 4a shows that a reconstructed thermal sequence image of the first principal component $PC1$, which contains most of the complete defect characteristic information of the 90 frames thermal sequence images. It is easy to identify the defect location. The reconstructed thermal sequence image of the second principal component $PC2$ is greatly affected by noise, and some defects are difficult to identify (see Figure 4b). In Figure 4c, the defect shape in the reconstructed thermal sequence image of the third principal component $PC3$ is severely distorted. Therefore, the reconstructed thermal sequence image of $PC1$ is selected for the following procedure. Line 1 marked by a dotted line in Figure 4a is used to the following quantitative analysis of defects.

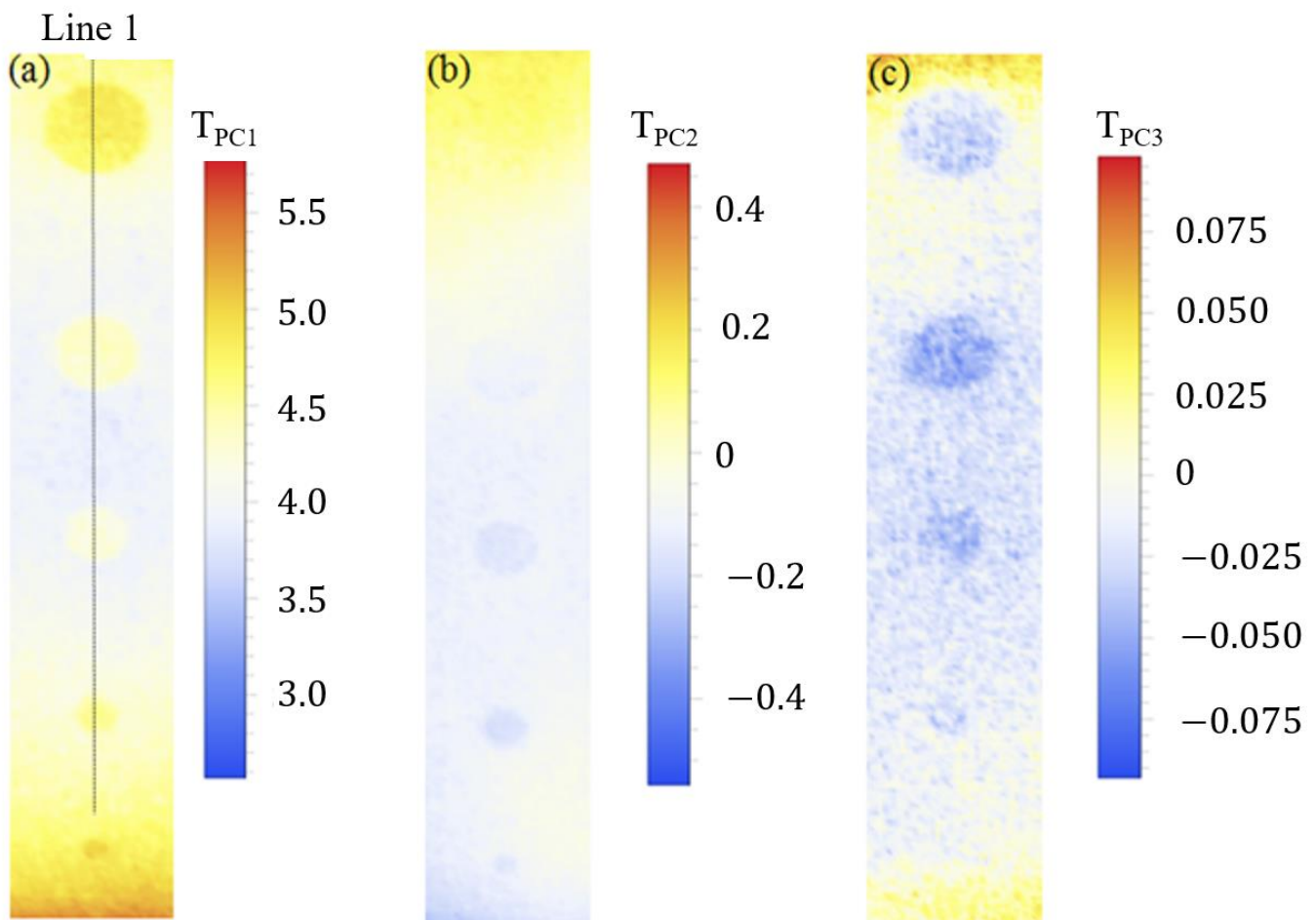


Figure 4. Reconstructed images by PCA algorithm of the sample 1: (a) PC1; (b) PC2; (c) PC3. Line 1 across the center of all flaws.

2.4. Subtracting Fitting Background

Two excitation lamps were placed symmetrically on both sides of the sample to reduce the effect of uneven heating. However, with the symmetrical distribution of the lamps, the effect of uneven heating was still existent. Figure 5 shows the temperature distribution along line 1 in Figure 4a. The temperature of the sample surface at the defect region is obviously higher than that at the intact region. Due to the uneven heating, the temperatures at both ends of the sample surface are higher, and the temperature in the central region is lower than that at both ends. To solve the adverse effect of uneven heating on defect detection, an image processing method of background subtraction is proposed in this section.

The process of subtracting fitting backgrounds consists of two steps: fitting background and background subtraction. Figure 6 shows the three-dimensional thermal images of flaw 1 in the sample 1. The three-dimensional size of defect can be identified as an abnormal rise region of temperature. The thermal data of the intact region is used to predict the thermal background in the defective region. A quadratic equation is proposed to fit the data of the thermal background:

$$T_{\text{fit}} = a + bx/l_p + c(x/l_p)^2 \quad (2)$$

where T_{fit} is the thermal background fitted by the thermal data of the intact region in Figure 6a. a , b , and c are the fitting parameters. x denotes the pixel points and l_p is one pixel. Next, we subtract the raw PCA image sequence T_{PC1} with the thermal background T_{fit} :

$$T_{Pf} = T_{PC1} - T_{fit} \tag{3}$$

where T_{Pf} is the thermal data in pixel points after subtracting the fitting background.

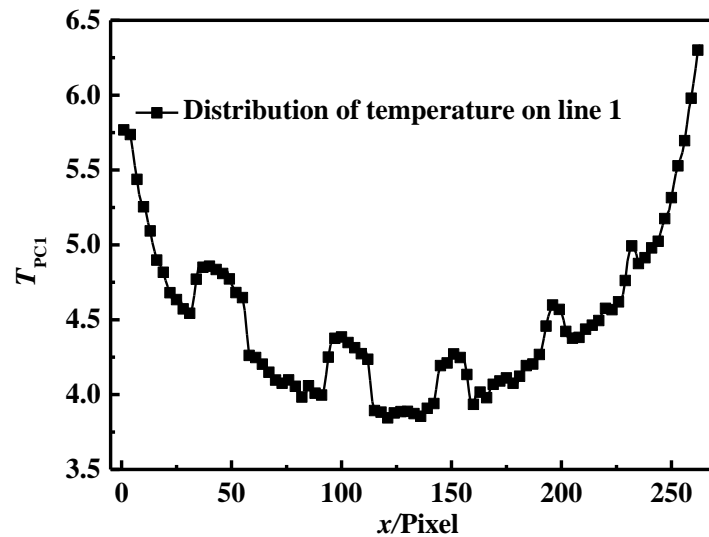


Figure 5. The temperature distribution along line 1 in Figure 4a.

Figure 6a shows a three-dimensional thermal image of PC1. The corresponding temperature values at two ends of the sample surface are different due to the uneven heating. To decrease this effect, a subtracting fitting background method is proposed. As shown in Figure 6b, a thermal image processed by the subtracting fitting background method can effectively reduce the local uneven heating noise. The processed images of this section are used to quantitative characterization analysis in the next section.

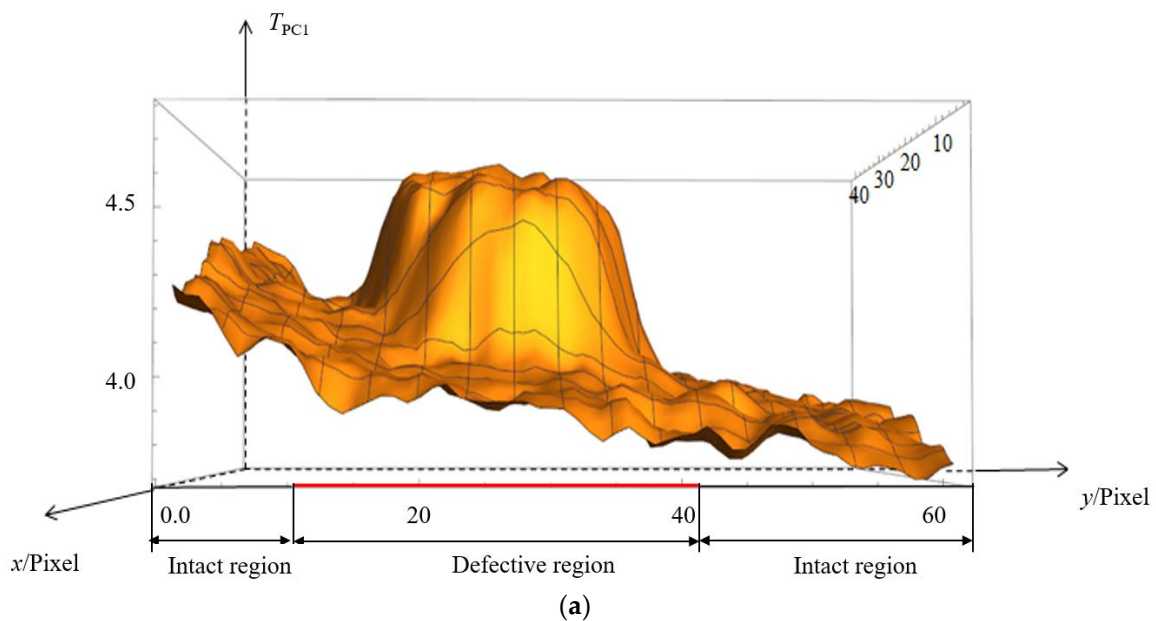


Figure 6. Cont.

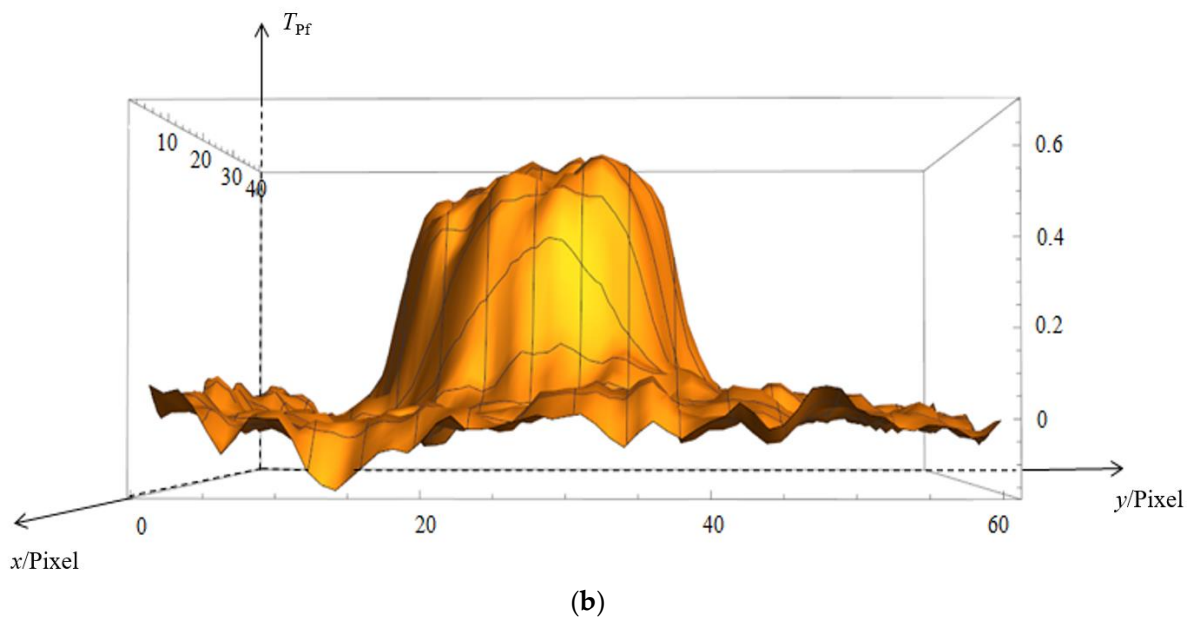


Figure 6. Three-dimensional thermal images of flaw 1 in the sample 1: (a) a raw thermal data extracted from PC1; (b) a thermal data extracted from PC1 after subtracting fitting background. Plane coordinates are represented by x -axis and y -axis. Vertical axis is used to record the value of temperature. Red line represents the coordinate range in y -axis, where the temperature has an abnormal rise.

3. Results and Discussion

3.1. Temperature Curve in the Defective Region after Subtracting the Fitting Background

To quantitatively analyze the lateral dimension of defects from the thermal images, the temperature distribution along line 1 was extracted from the thermal sequence image of PC1 after subtracting the fitting background. Figure 7 shows the temperature distribution in line 1 around defects with different diameters. The uneven background temperature can be effectively eliminated by algorithm processing of subtracting the fitting background. Due to the effect of the interface defect at the bottom of the ceramic coating on the distribution of the surface temperature of ceramic coating, the temperature in the defect area is higher than the intact region during the heating process by the heat source. After removing the source of motivation, the heat flows from the high temperature defect area to the low temperature intact area. Then, in collected infrared thermographs, the boundary of the high temperature area is fuzzy because the temperature changes from the heat flow. Also, the effect of interface defect on the transitive distance leads to the blurring of boundaries. Therefore, the sloping boundary of high-temperature area can be seen in Figure 7, and form the transition region between high and low temperature. When the lateral dimension of a defect is larger than 6 mm, the temperature distribution of the defective region presents a platform zone with undulating waveform. Note that the width of platform zone is a little less than the width of interfacial defect due to the transition region between high and low temperature. The width and height of the platform zone gradually decrease by decreasing the lateral dimension of a defect. When the lateral dimension of a defect is less than 6 mm, the transition regions distributed in the both sides of the high temperature area infinitely approach. Then, the platform zone disappears and reduces to an arch. The width and height of the arch also gradually decrease with decreasing the lateral dimension of a defect.

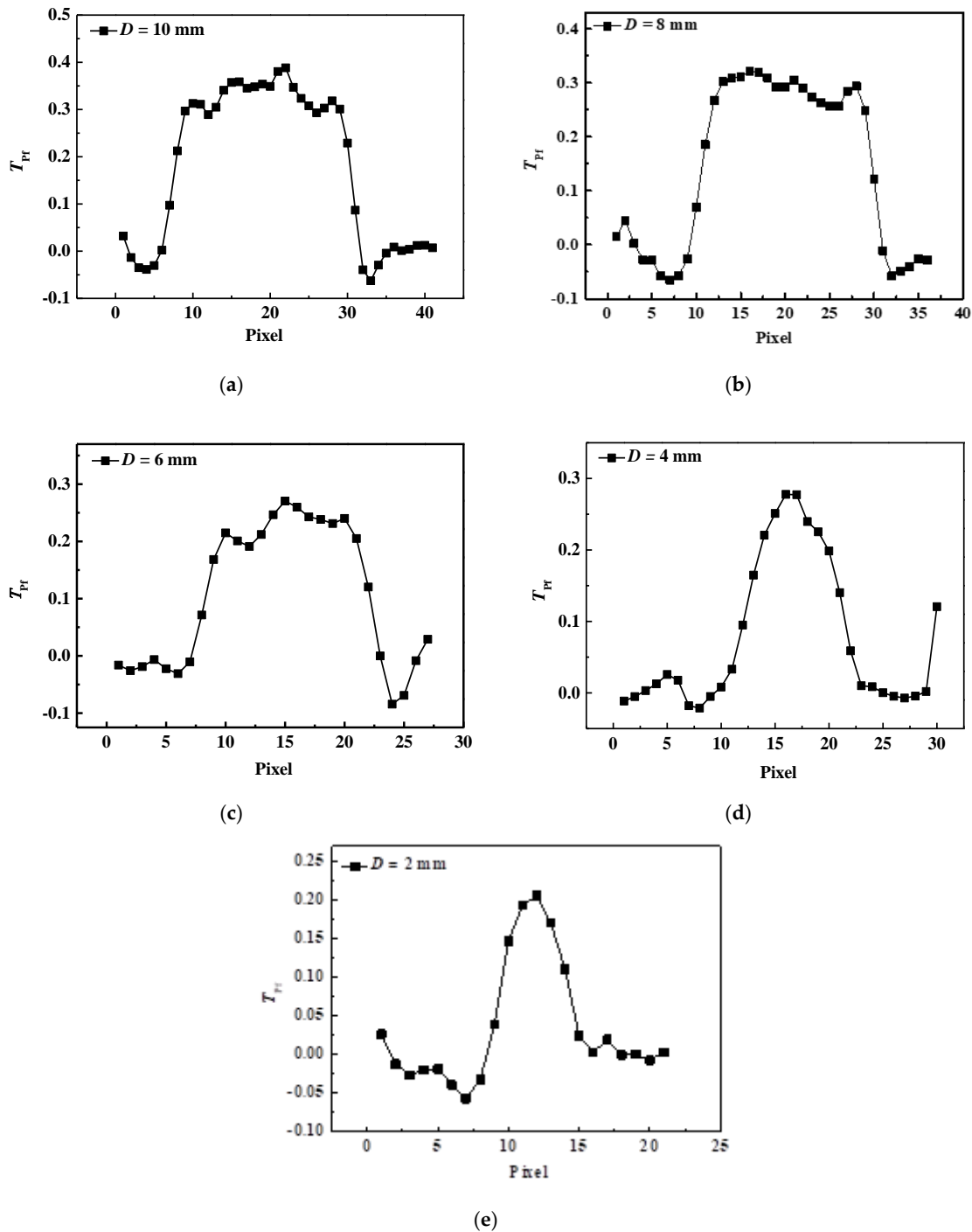


Figure 7. The temperature distribution around defects with different diameters after subtracting the fitting background: (a) $D = 10$ mm; (b) $D = 8$ mm; (c) $D = 6$ mm; (d) $D = 4$ mm and (e) $D = 2$ mm.

3.2. Heat Transfer Model of Interface Defect

The surfaces of defective and intact regions radiate heat outward during the sample heating by an excitation source. At the same time, the temperature difference between the defective region and the intact region leads the heat to flow transversely between the two regions (see Figure 8). Heat conduction can be represented by two processes, which are thermal diffusion in the vertical direction and transverse direction. According to the experimental results, the surface temperature of sample at the defective region is higher than that at the intact region during heating by an excitation source and cooling. Therefore, the temperature difference in the vertical direction is far less than that in the transverse

direction. Coating material at the defective region can be seen as a heat source when the excitation source is turned off. The temperature difference at the moment just turning off the excitation source is the most obvious. After a period of cooling, the temperature difference disappears gradually. In this work, we ignore the effect of heat diffusion in the vertical direction, and assume an ideal situation that the temperature on the surface of ceramic coating has a distribution as shown in Figure 9 at the moment just turning off the excitation source. The superscripts defect and intact represent variable in the defective and intact region.

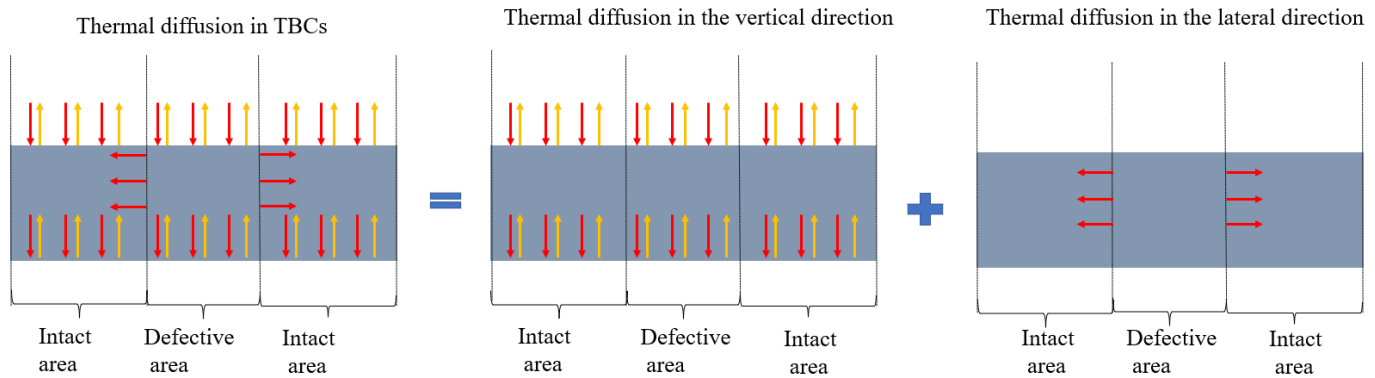


Figure 8. Schematic diagram of thermal diffusion in TBCs with interfacial defect.

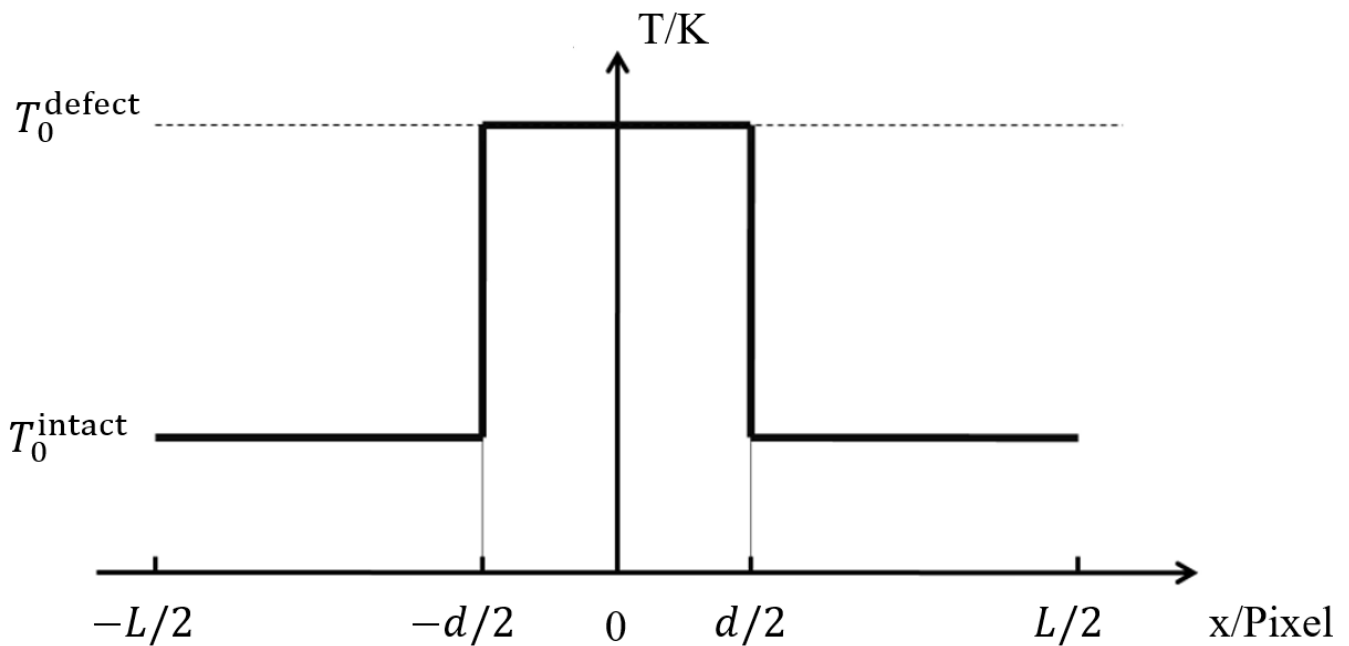


Figure 9. Temperature distribution on the surface of ceramic coating at the moment just turning off the excitation source.

A schematic diagram of heat conduction in the ceramic coating with interface defect during cooling process is shown in Figure 10. The differential equation of heat conduction on the surface of coating at the x axis direction is written as follows

$$\rho c \frac{\partial T_{\text{model}}(x, -e_1, t)}{\partial t} = \frac{\partial}{\partial x} \left(k_T \frac{\partial T_{\text{model}}(x, -e_1, t)}{\partial x} \right) \tag{4}$$

where ρ , c and k_T are the density, thermal capacity and the thermal diffusion coefficient of ceramic coating, respectively.

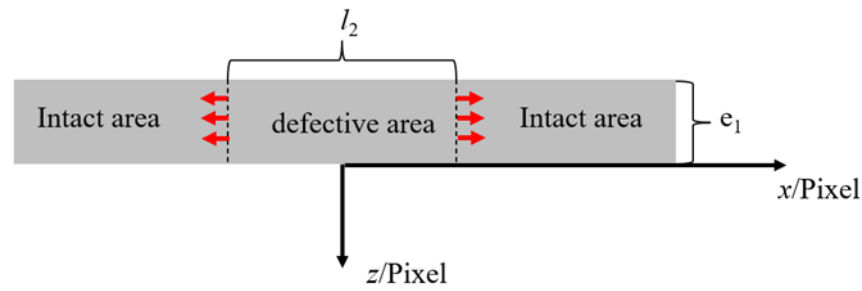


Figure 10. A schematic diagram of heat conduction in TBCs with defective area during cooling process. Red arrow denotes the direction of heat flow diffusion.

The initial condition and boundary condition are written as follows

$$T_{\text{model}}(x, -e_1, 0) = \phi(x) \tag{5}$$

$$T_{\text{model}}(-L/2, -e_1, t) = T_{\text{model}}(L/2, -e_1, t) = T_0^{\text{intact}} \tag{6}$$

where $\phi(x)$ is the temperature distribution on the surface of coating during cooling process and it presents a form of step function (see Figure 9). L and d are the length of the sample and the defect size in the model, respectively.

Then, an analytical expression of surface temperature can be derived as

$$T_{\text{model}}(x, -e_1, t) = \sum_{n=1}^k A_n \exp(-a^2(nw)^2t) \sin(nwx + \varphi) \tag{7}$$

$$A_n = \frac{2}{L} \int_{-L/2}^{L/2} \phi(x) \sin(nwx + \varphi) dx \quad n = 1, 2, 3, \dots, k$$

where a and φ are the constants. w is the fundamental frequency. Equation (7) is composed of cumulative sum and has a form of Fourier Series of $\phi(x)$.

After subtracting the fitting background, the temperature at the intact region T_0^{intact} is equal to zero. The temperature difference at the moment just turning off the excitation source is the most obvious. Then, we assume that the cooling time t is infinitely near zero. Then Equation (7) can be simplified as the discrete form of $\phi(x)$ and written as

$$T_{\text{model}} = T_0^{\text{defect}} + \sum_{n=1}^m T_0^{\text{defect}} a_n \cos(2nx\pi/L) + T_0^{\text{defect}} b_n \sin(2nx\pi/L) \quad \text{for } n = 1, 2, 3, \dots, m \tag{8}$$

$$a_n = \frac{1}{L} \int_{-L/2}^{L/2} T \cos(2nx\pi/L) dx$$

$$b_n = \frac{1}{L} \int_{-L/2}^{L/2} T \sin(2nx\pi/L) dx$$

Keep the value m as five, the variation of temperature function curve with different values of d is shown in Figure 11. It is worth noting that the changing trend of the temperature function curves with the decrease of d is the same as that shown in Figure 7. When the value of d is larger than 12, the distribution of T_{model} at the area between $-d/2$ and $d/2$ presents a platform zone with undulating waveform. The width and height of the platform zone gradually decrease with decreasing d . When the value of d is less than 12, the platform zone reduces to an arch. After that, the width and height of the arch also gradually decrease with decreasing d .

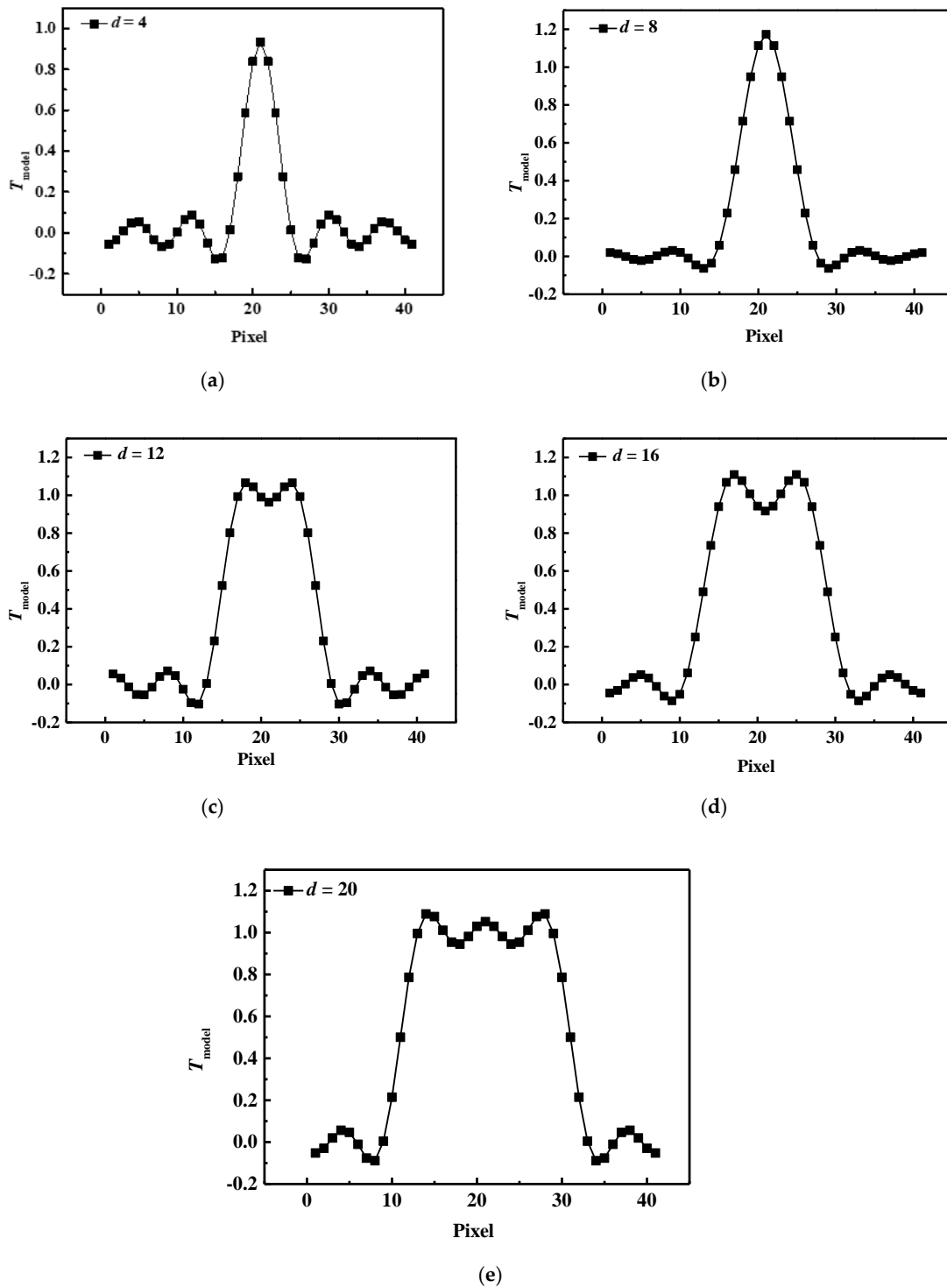


Figure 11. The discrete form of the Fourier series expansion of Equation (8) with different value of d : (a) $d = 4$ pixel; (b) $d = 8$ pixel; (c) $d = 12$ pixel; (d) $d = 16$ pixel and (e) $d = 20$ pixel.

3.3. Quantitative Analysis of Defect Size

Here we obtain the value of d corresponding to the defect size D of the flaw in sample 1 by editing the arithmetic to fit the Equation (8), with temperature curve shown in Figure 7. It should be noted that the change of curve shape from platform zone to arch with the decrease of d is remarkable, as shown in Figures 7 and 11. Therefore, only the change of the curve shape with different d is used to identify the corresponding D in this work. To avoid the effect of height difference between function curve of the model and temperature curve

of the experiment on quantitative analysis of defect size, we make the parameter T_0^{defect} automatically achieve the best match when the value of d is fixed.

Figure 12 gives the temperature curves of the experiment and the corresponding function curves with different d . R-square is used to represent the degree of fitting between curves of the model and the experiment. The right of Figure 12a shows the values of R-square with different value of d when D is equal to 10 mm. R-square has a maximum value of 0.98 when d is equal to 11.4. The left of Figure 12a gives the temperature curves of the experiment and best matched function curve. It is worth noting that the two curves do not have good match in the platform zone of temperature curves due to the uncontrollable effect of noise in infrared thermal image. For the rest of the defect size, the determination process of corresponding d is the same as that of $D = 10$ mm. When the maximal degree of fitting in function curves is achieved, d can be confirmed for each temperature curve. Figure 13 shows that the relationship between D , and d is directly proportional, approximatively. The linear fitting formula can be written as follows:

$$D/l_m = 0.49323 + 1.0812d/l_p \tag{9}$$

where l_m is equal to 1 mm and l_p is one pixel. Therefore, based on the directly proportional relationship between D and d , quantitative analysis of defect size by surface temperature at the defective region is feasible.

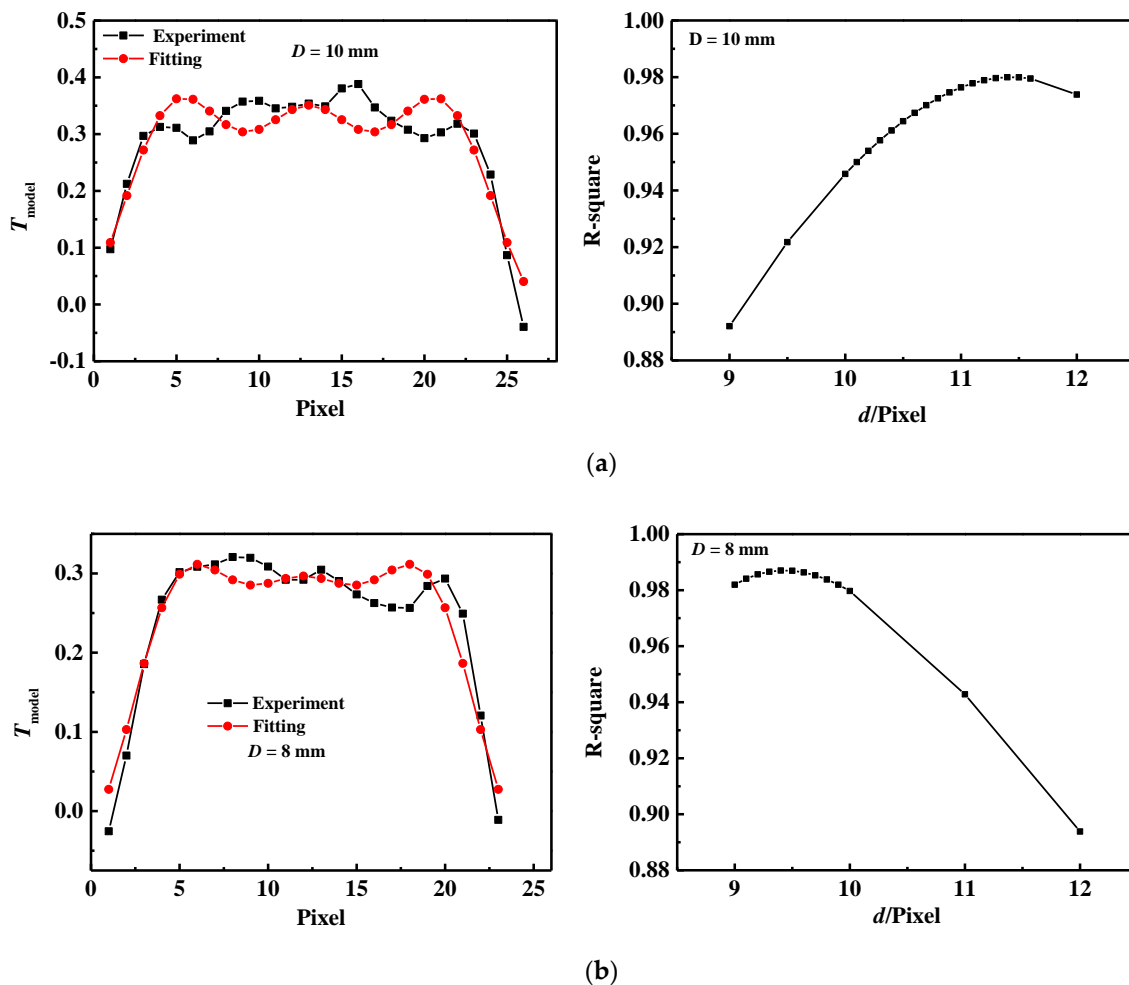


Figure 12. Cont.

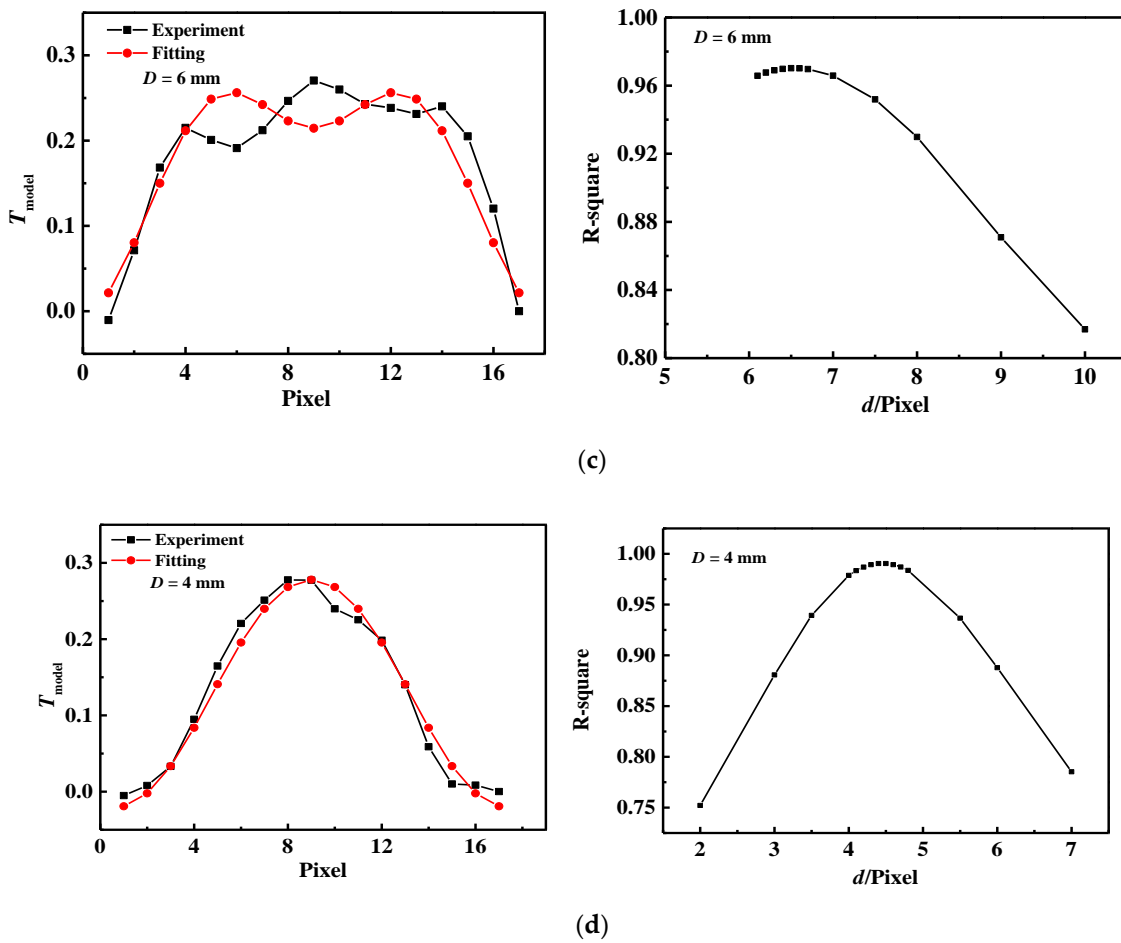


Figure 12. Temperature curve along the center of defect after background processing and fitted function curve with best degree of fitting (left). Degree of fitting of function curve vs. different value of d (right): (a) $D = 10$ mm; (b) $D = 8$ mm; (c) $D = 6$ mm and (d) $D = 4$ mm.

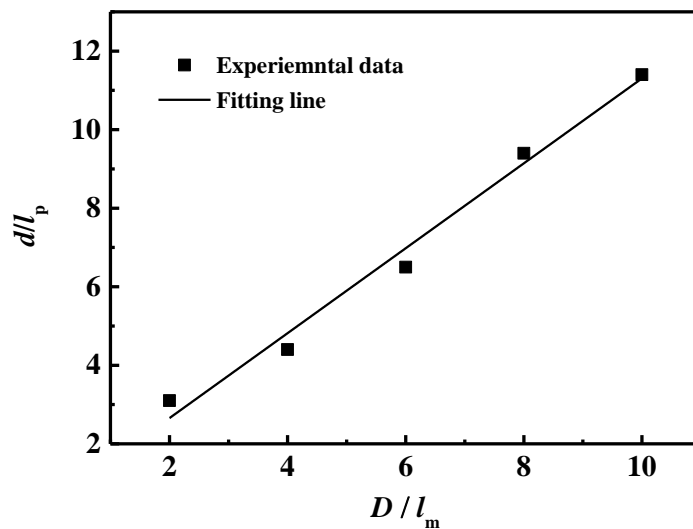


Figure 13. The defect size vs. the value of model parameter d .

Now, the defect size in the sample 2 can be estimated by using the aforementioned image manipulation and Equation (9). Firstly, the thermal image of defect in the sample 2 is dealt with in three processes: subtracting background image, PCA, and subtracting fitting background. Secondly, the temperature curve in the line across the center of the three flaws

is extracted. The parameter d is determined by edited arithmetic fitting the Equation (8) with the extracted temperature curve. At last, the predicted defect diameter in sample 2 is obtained by Equation (9). Table 3 gives the predicted diameter and actual diameter of defect in sample 2. For the defect with diameters of 3 mm, 5 mm, and 7 mm, the predicted defect diameters are 3.1509 mm, 4.7232 mm, and 7.2205 mm. It should be noted that the predicted errors are roughly distributed in the range of 3~6%, which are not affected by defect diameter. Table 4 gives the measuring error of the interfacial defect size in TBCs predicted by the method of Guo et al. [27] is larger than 12%. The error sharply increases with the decrease of the size of defect. When the defect diameter is 3 mm, the error reaches 25%. Compared with the results obtained by Guo et al. [27], the proposed model in this work can give a more accurately evaluation of the interfacial defect size in TBCs by the collected thermal image.

Table 3. The predicted diameter and actual diameter of defect in this work.

The Actual Defect Diameter (mm)	The Predicted Defect Diameter (mm)	Error
3	3.1509	5%
5	4.7232	5.5%
7	7.2205	3.2%

Table 4. The predicted diameter and actual diameter of the prepared interfacial defect in TBCs measured by the method of Guo et al. [27].

The Actual Defect Diameter (mm)	The Predicted Defect Diameter (mm)	Error
3	2.53	25%
5	4.55	15.4%
7	6.52	12%

Ideally, the proposed method in this work can give a more accurate result for the diameter of round interfacial defects when enough training data are used to determine the parameter in Equation (9). Due to the inevitable effect of noise in infrared thermal images, this method may fail when the defect size is too small to identify. At this time, the improvement on the resolution of infrared cameras can break this limit. Furthermore, the size of interfacial defect cannot be determined directly by the proposed method when the defect shape is not regular. This is another limitation of this evaluation method. In order to solve this problem, a simple extension of the proposed method is presented. As shown in Figure 14, a defect with irregular shape is divided into different areas by five black lines. The distance between two adjacent lines is same, which is denoted by M . The points of intersection between the defect profile and these lines are represented by solid black dots. The distance between the solid dot A and B is determined by the proposed method in this work (Note that the distance between the solid dot A and B corresponds to diameter D of round defect). The same operation is used to determine the distance between the solid dots in the rest of the lines. After that, the solid dots are connected by red lines, then a red broken line that replaces the defect profile is extracted (see Figure 14). Here, we use the area surrounded by red broken line to estimate the defect area, which can be divided into four trapezoidal regions by the five black lines. The lengths of the upper side and lower side for each of trapezoidal regions are determined by the proposed method in this work, then the area surrounded by red broken line can be obtained eventually. It is worth noting that the red broken line will be closer to the defect profile when more black lines are used to split the defect area. Therefore, a more accurate assessment of the area size of defect with irregular shape can be obtained, as shown in Figure 15.

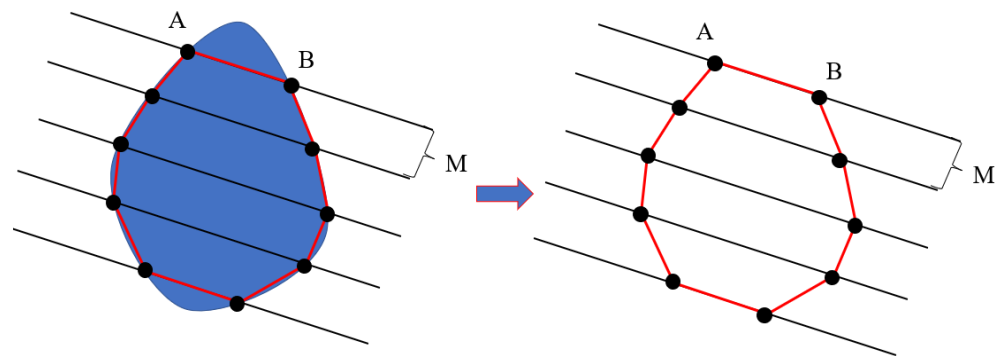


Figure 14. Schematic diagram of irregular defect. Five equidistant black lines are used to divide the area of irregular defect. A red broken line is extracted to replace the irregular defect profile.

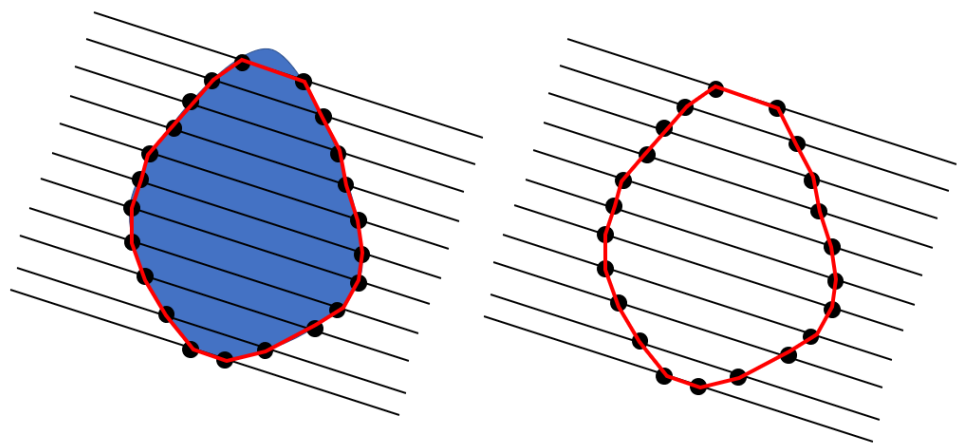


Figure 15. Schematic diagram of irregular defect. Eleven equidistant black lines are used to divide the area of irregular defect. A red broken line is extracted to replace the irregular defect profile.

4. Conclusions

In this work, the size of interface defects in TBCs is evaluated quantitatively by LPT. PCA and the method of background subtraction is proposed for improving the contrast of defects in collected infrared thermal image. The shapes of extracted temperature curves in the defective region change from platform to arch with the decrease in defect diameter. Based on the change rule of the shapes, an algorithm is edited to find the best matching result between the profile of interface defect in thermal images and the predicted shape of the model, and the interface defect size can be determined. For a defect with diameters of 3 mm, 5 mm, and 7 mm, the predicted defect diameters are 3.1509 mm, 4.7232 mm, and 7.2205 mm. The predicted errors are roughly distributed in the range of 3%~6%, which are not affected by the defect diameter. Furthermore, a simple extension of the proposed method to evaluate the size of the irregular shape defect is presented. A reconstructed broken line is presented to replace the irregular defect profile, and the area surrounded by the broken line can be estimated by the proposed method. Ideally, the broken line can be infinitely close to the defect profile when sufficient lines are used to split the defect area.

Author Contributions: Conceptualization, G.X. and W.Z.; Formal analysis, G.X. and G.L.; Funding acquisition, W.Z.; Investigation, J.W., G.X. and J.G.; Methodology, J.W. and W.Z.; Resources, J.G. and Z.M.; Software, J.W., G.L. and J.G.; Supervision, W.Z.; Validation, G.L. and Z.M.; Writing—original draft, J.W. and G.X.; Writing—review & editing, J.G. and W.Z. All authors have read and agreed to the published version of the manuscript.

Funding: This work was supported by the Science and Technology Innovation Program of Hunan Province (Grant No. 2022RC1082), the Natural Science Foundation of Hunan Province (Grant No. 2020JJ3031), the Scientific Research Foundation of Hunan Provincial Education Department (Grant

No. 21A0120) and Postgraduate Scientific Research Innovation Project of Hunan Province (Grant No. XDCX2021B145).

Institutional Review Board Statement: Not applicable.

Informed Consent Statement: Not applicable.

Data Availability Statement: Not applicable.

Conflicts of Interest: The authors declare that they have no known competing financial interests or personal relationships that could have appeared to influence the work reported in this paper.

References

1. Darolia, R. Thermal barrier coatings technology: Critical review, progress update, remaining challenges and prospects. *Int. Mater. Rev.* **2013**, *58*, 315–348. [[CrossRef](#)]
2. Vo, D.T.; Mai, T.D.; Kim, B.; Ryu, J. Numerical study on the influence of coolant temperature, pressure, and thermal barrier coating thickness on heat transfer in high-pressure blades. *Int. J. Heat Mass Transf.* **2022**, *189*, 122715. [[CrossRef](#)]
3. Pan, W.; Phillpot, S.R.; Wan, C.; Chernatynskiy, A.; Qu, Z. Low thermal conductivity oxides. *MRS Bull.* **2012**, *37*, 917–922. [[CrossRef](#)]
4. Feuerstein, A.; Knapp, J.; Taylor, T.; Ashary, A.; Bolcavage, A.; Hitchman, N. Technical and economical aspects of current thermal barrier coating systems for gas turbine engines by thermal spray and EB-PVD: A review. *J. Therm. Spray Technol.* **2008**, *17*, 199–213. [[CrossRef](#)]
5. Padture, N. Advanced structural ceramics in aerospace propulsion. *Nat. Mater.* **2016**, *15*, 804. [[CrossRef](#)]
6. Benini, B. *Progress in Gas Turbine Performance*; BoD-Books on Demand; IntechOpen: London, UK, 2013.
7. Jonnalagadda, K.P.; Eriksson, R.; Li, X.-H.; Peng, R.L. Thermal barrier coatings: Life model development and validation. *Surf. Coat. Technol.* **2019**, *362*, 293–301. [[CrossRef](#)]
8. Padture, N.P.; Gell, M.; Jordan, E.H. Thermal barrier coatings for gas-turbine engine applications. *Science* **2002**, *296*, 280–284. [[CrossRef](#)]
9. Zhen, Z.; Wang, X.; Shen, Z.; Mu, R.; He, L.; Xu, Z. Thermal cycling behavior of EB-PVD rare earth oxides co-doping ZrO₂-based thermal barrier coatings. *Ceram. Int.* **2021**, *47*, 23101–23109. [[CrossRef](#)]
10. Wei, Z.-Y.; Cai, H.-N.; Zhao, S.-D. Study on spalling mechanism of APS thermal barrier coatings considering surface vertical crack evolution affected by surrounding cracks. *Ceram. Int.* **2022**, *48*, 11445–11455. [[CrossRef](#)]
11. Choi, S.R.; Hutchinson, J.W.; Evans, A.G. Delamination of multilayer thermal barrier coatings. *Mech. Mater.* **1999**, *31*, 431–447. [[CrossRef](#)]
12. Mao, W.; Dai, C.; Zhou, Y.; Liu, Q. An experimental investigation on thermomechanical buckling delamination failure characteristic of air plasma sprayed thermal barrier coating. *Surf. Coat. Technol.* **2007**, *201*, 6217–6227. [[CrossRef](#)]
13. Ma, Z.; Sun, L.; Chen, Y.; Lin, L. Ultrasonic prediction of thermal barrier coating porosity through multiscale-characteristic-based Gaussian process regression algorithm. *Appl. Acoust.* **2022**, *195*, 108831. [[CrossRef](#)]
14. Yang, X.; Wei, L.; Li, J.; Zhang, B.; Wang, S.; Guo, H. Microstructural evolution of plasma spray physical vapor deposited thermal barrier coatings at 1150 °C studied by impedance spectroscopy. *Ceram. Int.* **2018**, *44*, 10797–10805. [[CrossRef](#)]
15. Ahmadian, S.; Browning, A.; Jordan, E.H. Three-dimensional X-ray micro-computed tomography of cracks in a furnace cycled air plasma sprayed thermal barrier coating. *Scr. Mater.* **2015**, *97*, 13–16. [[CrossRef](#)]
16. Zhu, W.; Cai, X.; Yang, L.; Xia, J.; Zhou, Y.; Pi, Z. The evolution of pores in thermal barrier coatings under volcanic ash corrosion using X-ray computed tomography. *Surf. Coat. Technol.* **2019**, *357*, 372–378. [[CrossRef](#)]
17. Li, Y.; Song, Y.; Yang, Z.; Xie, X. Use of line laser scanning tomography for the defect detection and evaluation of composite material. *Sci. Eng. Compos. Mater.* **2022**, *29*, 74–83. [[CrossRef](#)]
18. Zhu, J.; Mao, Z.; Wu, D.; Zhou, J.; Jiao, D.; Shi, W.; Zhu, W.; Liu, Z. Progress and trends in non-destructive testing for thermal barrier coatings based on infrared thermography: A review. *J. Nondestruct. Eval.* **2022**, *41*, 1–26. [[CrossRef](#)]
19. Cernuschi, F.; Bison, P. Thirty Years of Thermal Barrier Coatings (TBC), Photothermal and thermographic techniques: Best practices and lessons learned. *J. Therm. Spray Technol.* **2022**, *31*, 716–744. [[CrossRef](#)]
20. Kessler, S.S.; Spearing, S.M.; Soutis, C. Damage detection in composite materials using Lamb wave methods. *Smart Mater. Struct.* **2002**, *11*, 269. [[CrossRef](#)]
21. Newaz, G.; Chen, X. Progressive damage assessment in thermal barrier coatings using thermal wave imaging technique. *Surf. Coat. Technol.* **2005**, *190*, 7–14. [[CrossRef](#)]
22. Unnikrishnakurup, S.; Dash, J.; Ray, S.; Pesala, B.; Balasubramaniam, K. Nondestructive evaluation of thermal barrier coating thickness degradation using pulsed IR thermography and THz-TDS measurements: A comparative Study. *NDT E Int.* **2020**, *116*, 102367. [[CrossRef](#)]
23. Kumar, M.M.; Pavan, A.; Markandeya, R.; Singh, K. Defect assessment in gas turbine blade coatings using non-contact thermography. *Mater. Today: Proc.* **2021**, *44*, 4414–4420.
24. Shi, L.; Long, Y.; Wang, Y.; Chen, X.; Zhao, Q. Online nondestructive evaluation of TBC crack using infrared thermography. *Meas. Sci. Technol.* **2021**, *32*, 115008. [[CrossRef](#)]

25. Zhu, W.; Li, Z.Y.; Yang, L.; Zhou, Y.C.; Wei, J.F. Real-time detection of CMAS corrosion failure in APS thermal barrier coatings under thermal shock. *Exp. Mech.* **2020**, *60*, 775–785. [[CrossRef](#)]
26. Zhuo, L.; Yang, X.; Zhu, J.; Huang, Z.; Chao, J.; Xie, W. Size determination of interior defects by reconstruction of subsurface virtual heat flux for step heating thermography. *NDT E Int.* **2022**, *133*, 102734. [[CrossRef](#)]
27. Guo, W.; Dong, L.; Wang, H.; Feng, F.; Xing, Z.; Ma, R.; Shao, H.; Gao, Z.; Wang, B.; Yang, J. Size estimation of coating disbands using the first derivative images in pulsed thermography. *Infrared Phys. Technol.* **2020**, *104*, 103106. [[CrossRef](#)]
28. Rajic, N. Principal component thermography for flaw contrast enhancement and flaw depth characterization in composite structures. *Compos. Struct.* **2002**, *58*, 521–528. [[CrossRef](#)]
29. Balageas, D.L.; Roche, J.-M.; Leroy, F.-H.; Liu, W.-M.; Gorbach, A.M. The thermographic signal reconstruction method: A powerful tool for the enhancement of transient thermographic images. *Biocybern. Biomed. Eng.* **2015**, *35*, 1–9. [[CrossRef](#)]
30. Marinetti, S.; Grinzato, E.; Bison, P.; Bozzi, E.; Chimenti, M.; Pieri, G.; Salvetti, O. Salvetti, Statistical analysis of IR thermographic sequences by PCA. *Infrared Phys. Technol.* **2004**, *46*, 85–91. [[CrossRef](#)]
31. Ibarra-Castanedo, C.; González, D.; Klein, M.; Pilla, M.; Vallerand, S.; Maldague, X. Infrared image processing and data analysis. *Infrared Phys. Technol.* **2004**, *46*, 75–83. [[CrossRef](#)]
32. Wang, Z.; Zhu, J.; Tian, G.; Ciampa, F. Ciampa, Comparative analysis of eddy current pulsed thermography and long pulse thermography for damage detection in metals and composites. *NDT E Int.* **2019**, *107*, 102155. [[CrossRef](#)]